Key Points:
- We detect 32,078 very small, local microearthquakes at TAG active mound
- We model earthquakes as reaction-driven fracturing from anhydrite deposition
- Events reveal shallow secondary circulation system of the hydrothermal mound

Correspondence to:
C. W. Pontbriand,
claire.wp@gmail.com

Microearthquake evidence for reaction-driven cracking within the Trans-Atlantic Geotraverse active hydrothermal deposit
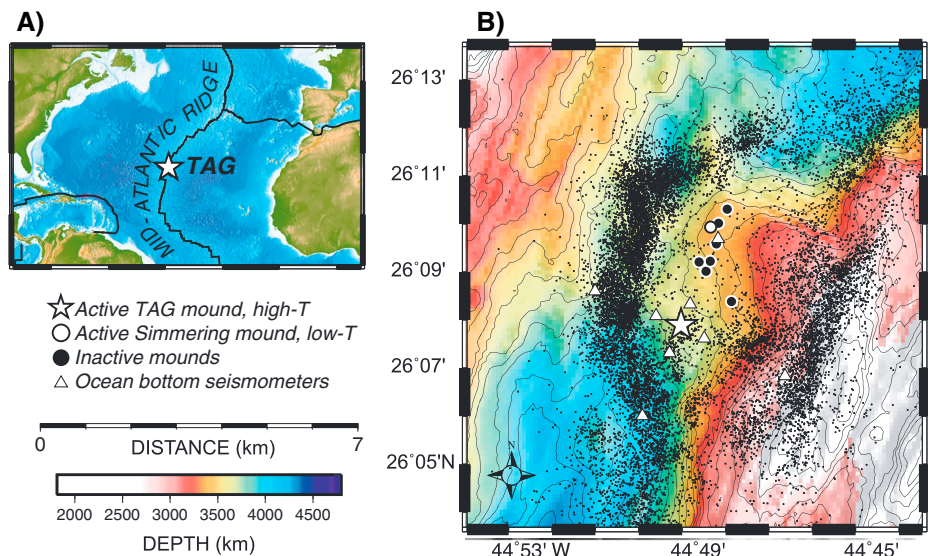
Claire W. Pontbriand[1] and Robert A. Sohn[2]

[1]MIT/WHOI Joint Program in Oceanography, Cambridge, Massachusetts, USA, [2]Woods Hole Oceanographic Institution, Woods Hole, Massachusetts, USA

Abstract We detected 32,078 very small, local microearthquakes (average $M_L = -1$) during a 9 month deployment of five ocean bottom seismometers on the periphery of the Trans-Atlantic Geotraverse active mound. Seismicity rates were constant without any main shock-aftershock behavior at ~243 events per day at the beginning of the experiment, 128 events per day after an instrument failed, and 97 events per day at the end of the experiment when whale calls increased background noise levels. The microearthquake seismograms are characterized by durations of <1 s and most have single-phase P wave arrivals (i.e., no S arrivals). We accurately located 6207 of the earthquakes, with hypocenters clustered within a narrow depth interval from ~50 to 125 m below seafloor on the south and west flanks of the deposit. We model the microearthquakes as reaction-driven fracturing events caused by anhydrite deposition in the secondary circulation system of the hydrothermal mound and show that under reasonable modeling assumptions an average event represents a volume increase of 31–58 cm^3, yielding an annual (seismogenic) anhydrite deposition rate of 27–51 m^3.

1. Introduction

Seafloor massive sulfide deposits are the modern equivalents of ancient ophiolite-hosted ore deposits, such as those mined for copper and gold in Cypress, Oman, and Newfoundland [*Humphris et al.*, 1995; *Hannington et al.*, 1998; *Humphris and Cann*, 2000]. The Trans-Atlantic Geotraverse (TAG) hydrothermal field on the Mid-Atlantic Ridge (MAR) at 26°N (Figure 1a) is the largest known deep-sea massive sulfide deposit, and it has been the focus of numerous geophysical [*Evans*, 1996; *Tivey et al.*, 2003; *Canales et al.*, 2007; *deMartin et al.*, 2007], geochemical [*Edmond et al.*, 1995; *Chiba et al.*, 1998; *Tivey et al.*, 1998; *Humphris and Tivey*, 2000; *Humphris and Bach*, 2005], and biological [*Van Dover et al.*, 1988; *Galkin and Moskalev*, 1990; *Van Dover*, 1995; *Copley et al.*, 1999] studies. The TAG field consists of one active high-temperature mound, one active low-temperature mound, and seven inactive high-temperature mounds spread across a 5×5 km^2 zone [*Rona et al.*, 1993a,1993b; *White et al.*, 1998] on the hanging wall of the active TAG detachment fault (Figure 1b) [*Tivey et al.*, 2003; *Canales et al.*, 2007, *deMartin et al.*, 2007]. Radiometric dating indicates that high-temperature discharge has shifted from mound to mound over the past ~100,000 years and that the presently active site has experienced pulses of activity every 4000–6000 years over the past ~20,000 years [*Lalou et al.*, 1990, 1993, 1998; *You and Bickle*, 1998].

Genesis of a seafloor massive sulfide deposit is associated with both a primary system of hydrothermal circulation that extracts heat from a deep magmatic source region and a secondary circulation system that entrains seawater to cool the shallow deposit [*Sleep*, 1991; *Tivey et al.*, 1995; *Lowell and Yao*, 2002; *Lowell et al.*, 2003]. Although the location of the deep-seated heat source driving primary circulation at TAG is unknown, it is constrained by seismic refraction data to lie below the hanging wall-footwall interface of the active detachment fault [*Canales et al.*, 2007; *Zhao et al.*, 2012] and therefore is several kilometer or more below the seafloor. Primary circulation in the middle-lower crust may be focused on the relatively permeable detachment fault interface, which extends to depths > 7 km below the seafloor [*deMartin et al.*, 2007], but in the upper crust high-temperature fluids must rise vertically through a highly fissured hanging wall. Focusing of hydrothermal activity into discrete mounds at the seafloor is believed to be controlled by permeable pathways formed by intersecting sets of faults and fissures [*Zonenshain et al.*, 1989; *Karson and Rona*, 1990; *Kleinrock and Humphris*, 1996].
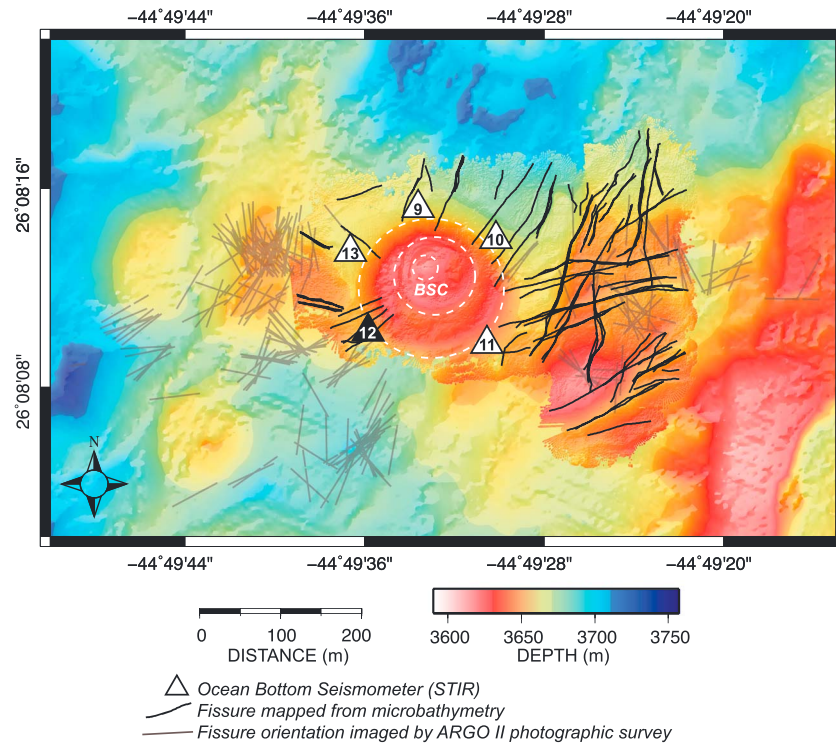
Figure 1. (a) Regional map of the Mid-Atlantic Ridge showing location of the TAG segment at 26°N. (b) Bathymetry of the TAG segment with microearthquake epicenters (black dots) from *deMartin et al.* [2007]. The hydrothermal field, consisting of relict and active deposits, is situated on the hanging wall of an active detachment fault [*Tivey et al.*, 2003; *deMartin et al.*, 2007].

The TAG active mound is a ~200 m diameter by ~50 m tall massive sulfide deposit with hydrothermal fluids discharging at temperatures in excess of 360°C and a total heat flux of ~1 GW [*Wichers et al.*, 2005]. High-temperature fluid discharge is focused in an ~80 m wide upflow zone to the black smoker complex (BSC), which constitutes a set of sulfide chimneys at the top of the mound [*Humphris and Kleinrock*, 1996; *Honnorez et al.*, 1998]. Lower temperature fluids, presumably resulting from mixing of high-temperature fluids with cold seawater, discharge from a multitude of locations on the mound [*Campbell et al.*, 1988; *Humphris et al.*, 1995; *Tivey et al.*, 1995]. The structure of the active sulfide deposit and the processes that have formed it are largely informed by a series of up to 125.7 m cores obtained during Ocean Drilling Program (ODP) Leg 158 [*Humphris et al.*, 1996; *Herzig et al.*, 1998a]. These cores revealed a complex, zoned subsurface stratigraphy resulting from low- and high-temperature water rock reactions, with an abundance of anhydrite deposited by interactions between hydrothermal fluid, entrained seawater, and stockwork [*Herzig et al.*, 1998b].

The active mound has developed as a breccia pile through periods of venting and quiescence over the past ~20,000 years [*Lalou et al.*, 1990; *Humphris and Kleinrock*, 1996], and it exhibits complex short-term space-time discharge patterns [*Sohn*, 2007a, 2007b]. Anhydrite, which is retrograde soluble, is continually precipitated in shallow subsurface flow conduits as seawater entrained in a secondary circulation system is heated to temperatures of ~160°C or more, either through conductive heating or mixing with hydrothermal fluids [*Chiba et al.*, 1998; *Mills et al.*, 1998; *Teagle et al.*, 1998]. By contrast, anhydrite dissolves during periods of quiescence in response to cooling, leading to mass wasting and extensive reworking of the sulfides. Deposition and dissolution of anhydrite are thus key processes in the genesis and evolution of the massive sulfide mound, but our understanding of them is largely limited to inferences from a few short drill cores. In particular, the geometry and subsurface extent of anhydrite beneath the active mound are largely unknown, as are the primary flow paths for the secondary circulation system, which likely represent the loci of anhydrite deposition at any given time.

Here we present results from a 9 month deployment of a small-aperture (~200 m) network of five ocean bottom seismometers (OBSs) on the perimeter of the TAG active mound. The small-aperture OBS network was designed to image very small microearthquakes triggered by hydrothermal processes within the hydrothermal deposit. OBS deployments in hydrothermal areas typically observe high levels of microearthquake activity generated by magmatic and tectonic processes associated with mid-ocean ridge volcanic centers [e.g., *Sohn et al.*, 1999; *Wilcock et al.*, 2002; *Bohnenstiehl, et al.*, 2008], but our study represents the first time that a small-aperture OBS network has been deployed on the scale of an individual hydrothermal mound. As a result, we have the ability to detect and locate very small microearthquakes associated with
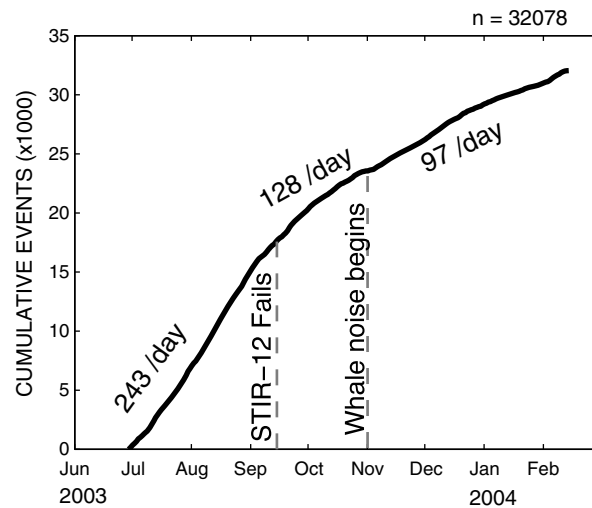
Figure 2. Microbathymetry of the TAG active mound [*White et al.*, 1998; *Roman and Singh*, 2007]. The surface expression of the ~200 m diameter mound is indicated by the outermost dashed white circle. High-temperature discharge (>360°C) during the time period of the STAG experiment was focused at the black smoker complex (BSC), whereas low-temperature (<100°C) discharge was observed at discrete locations across the upper terrace [*Sohn*, 2007a]. Locations of the five OBSs on the periphery of the mound are denoted by triangles. STIR-12 (black triangle) failed 77 days into the experiment. Local fault/fissure orientations show great variation [*Bohnenstiehl and Kleinrock*, 2000].

intrinsic hydrothermal processes such as hydraulic fracturing within the deposit, which has provided valuable information regarding the shallow hydrogeology of geothermal fields on land [e.g., *Bame and Fehler*, 1986; *Ferrazzini et al.*, 1990; *Kedar et al.*, 1996, 1998; *Bianco et al.*, 2004; *Foulger et al.*, 2004]. With network interelement spacings as small as 98 m we are able to detect 32,078 microearthquakes with an average size of $M_L = -1$ and accurately locate 6207 of these events. We find that the hypocenters cluster on to the south and west of the mound and occur within a narrow depth interval from ~50 to 125 m below the seafloor. We model the microearthquakes as reaction-driven fracturing events in response to the deposition of anhydrite in the secondary circulation system and use this model to constrain the rate and subsurface location of anhydrite deposition at the active mound.

2. Experiment and Data Analysis

An OBS network was deployed at the TAG segment of the MAR from June 2003 to February 2004 as part of the seismicity and fluid flow of the TAG (STAG) hydrothermal mound experiment (Figure 2a). The OBS network consisted of three rings of instruments centered on the active hydrothermal mound with apertures of 200 m, 2 km, and 8 km, respectively. Here we report analyses and results from the smallest aperture subnetwork (the "inner ring"), which was deployed around the periphery of the TAG active mound in an attempt to record very small microearthquakes associated with fluid flow in the deposit (Figure 2). The subnetwork consisted of five WHOI D2 OBSs, which are four-component (3 geophone + 1 hydrophone channel), short-period (4.5 Hz natural frequency) instruments. The seismometers recorded continuous data at 100 Hz for the 9 month duration of the deployment, except for STIR-12, which failed 77 days into the study for unknown reasons. The instruments were deployed by wire (rather than free-fall) from the R/V *Knorr* and released from an altitude ~15 m above the seafloor using an acoustic release system. The seafloor position of the instruments was estimated using a relay transponder and long baseline navigation techniques to an

Figure 3. Cumulative events (total = 32,078) versus time. Event rate is 243 per day until STIR-12 fails 77 days into the study, at which point the apparent rate reduces to 128 per day as a result of the loss of data. The apparent rate decreases to 97 per day when whale calls increase background noise levels.

accuracy of a few meters. Three of the OBSs were visited during *Alvin* dives, which allowed for verification of seafloor position and visual inspection of landing position/coupling of the OBSs.

We present analyses for those microearthquakes that were *only* detected on the inner ring OBSs. The inner ring instruments detected large numbers of events that were also detected on the larger-scale subnetworks [*deMartin et al.*, 2007], but we exclude those events from our analyses in order to focus on seismic activity within the hydrothermal deposit. We further restrict our analyses to those events that were detected by at least four inner ring instruments in order to have sufficient degrees of freedom to constrain hypocentral parameters. We picked arrivals for 32,078 microearthquakes fitting these criteria using a

short-term-average to long-term-average (STA/LTA) algorithm with parameters optimized via comparison with handpicked events on random data windows. We then used the optimized STA/LTA parameters (STA/LTA > 2.2 for window lengths of 0.2 s and 10 s, respectively) to automatically detect events for the entire data set. We refined the arrival time picks using spectral methods [e.g., *Song et al.*, 2010]. Linear clock drift corrections were applied to each station, and these corrections were further refined to account for nonlinear clock drift by cross-correlating long-wavelength (0.1–5 Hz) microseism signals [*Webb*, 1992; *Webb and Crawford*, 1999] that propagated across the small-aperture subnetwork during various times throughout the experiment (supporting information). Finally, station corrections were applied to each record by subtracting the mean arrival time residual for all events (−6.5 ms for STIR-9, −0.2 ms for STIR-10, 0.5 ms for STIR-11, 2.0 ms for STIR-12, and −7.2 ms for STIR-13).

Hypocenters were estimated using a stochastic grid search routine [e.g., *Sohn et al.*, 1998] minimizing root mean square (RMS) traveltime residuals between the phase picks and raytracing predictions over a 1.2 km cubic grid with 40 m node spacing. We used the average seismic (*P* wave) velocity versus depth profile for the TAG region from *Canales et al.* [2007] as a starting point for developing a raytracing velocity model. Because the seismic velocities in the shallow-most crust (i.e., extrusive lithologies in seismic layer 2A) are not well constrained in the *Canales et al.* [2007] model, we systematically perturbed the shallow velocities and selected the model that minimized hypocentral errors for a subset of 1000 randomly selected events. Our final model has a *P* wave velocity of 2.5 km s^{-1} at the seafloor that increases linearly with depth to a velocity of ~4 km s^{-1} at 1 km below the seafloor, and it is draped over the local bathymetry, including the active mound [*White et al.*, 1998; *Roman and Singh*, 2007]. Microearthquake moments and local magnitudes were calculated using standard techniques [e.g., *Deichmann*, 2006].
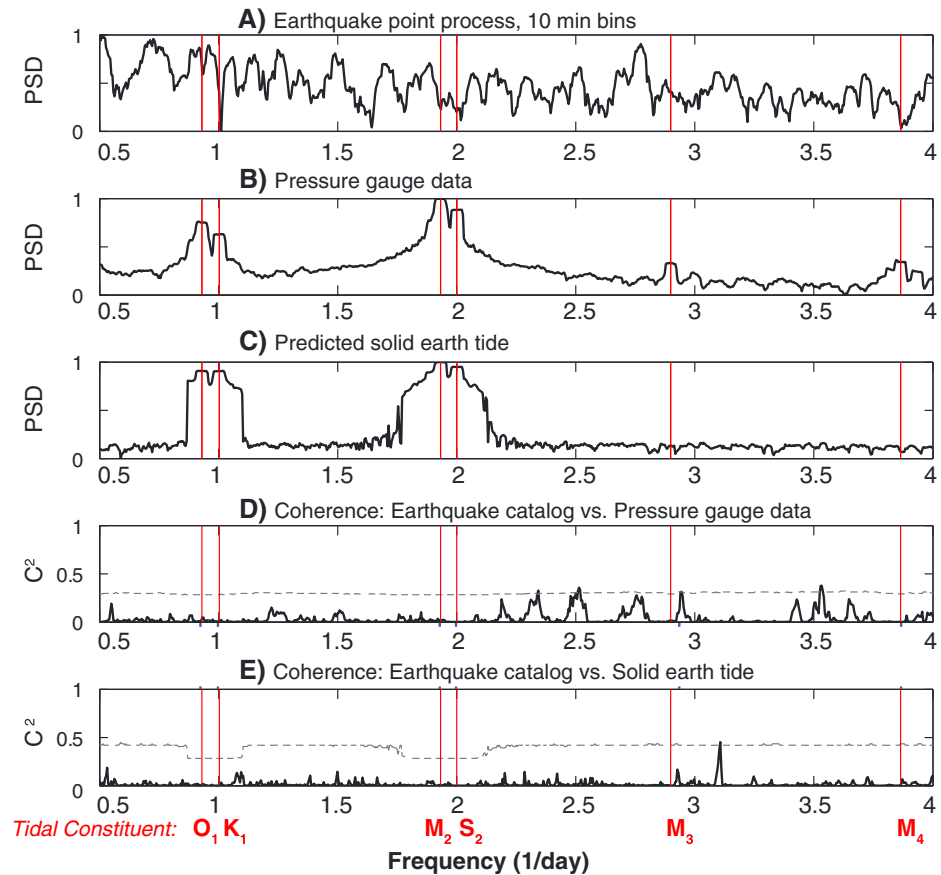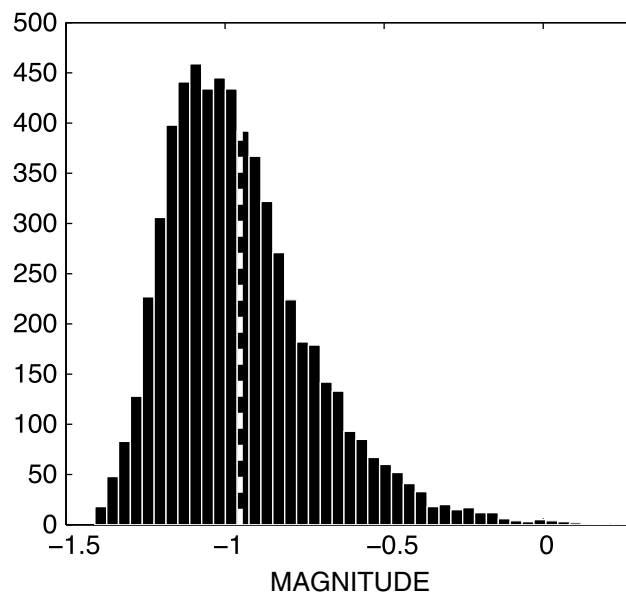
3. Results

We detected 32,078 events detected during the 9 month OBS deployment. Seismicity rates during the deployment were essentially constant, although the rate decreased from 243 to 128 microearthquakes per day when STIR-12 failed 77 days into the experiment and then decreased again to 97 events per day when whale calls [e.g., *McDonald et al.*, 1995] increased background noise levels in the study area (Figure 3). The microearthquakes do not exhibit main shock-aftershock sequences, swarm-like behavior, nor evidence for migration. The coefficient of variation [*Kagan and Jackson*, 1991] for the microearthquake catalog is 1.2, indicating that the event times are nearly random (i.e., Poisson process) with only a small degree of temporal clustering. The source process rate was thus essentially constant during the experiment, with very little interaction/triggering between the events.
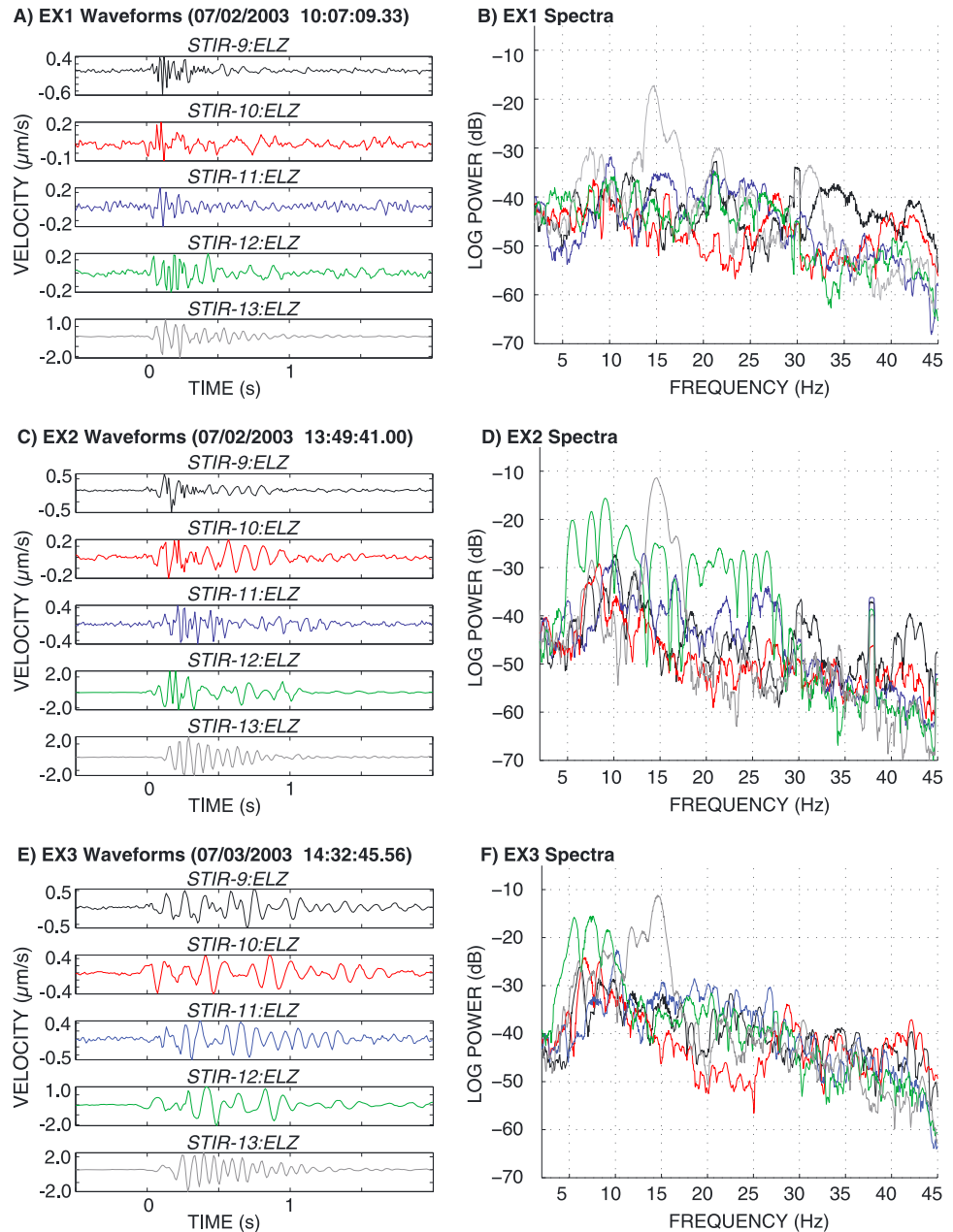
Figure 4. Normalized multitaper spectral estimates (NW = 5) of (a) the microearthquake catalog as a point process (10 min bins), (b) ocean tidal loading (pressure gauge) data [c.f. *Sohn et al.*, 2009], and (c) predicted solid Earth tide loading [*Matsumoto et al.*, 2001]. Frequencies of the major tidal constituents (O_1, K_1, M_2, S_2, M_3, M_4) are indicated with blue lines [*Foreman*, 1977]. Cross-spectral coherency between the microearthquake catalog and (d) the measured ocean tide and (e) the predicted solid earth tide. The zero significance level (i.e., coherencies less than or equal to this value are not statistically distinguishable from zero at the 95% confidence level) is shown as a dashed grey line [*Percival and Walden*, 1993].

Figure 5. Magnitude histogram of 6207 well-located events (RMS error < 20 ms). Mean local magnitude is −0.95 and mean log moment is 14.57 ($\log_{10}$ dyn cm).

We investigated the possibility of tidal triggering, which has been reported for some mid-ocean ridge (MOR) micro-earthquake studies [e.g., *Wilcock*, 2001; *Tolstoy et al.*, 2002, 2008; *Stroup et al.*, 2007] by estimating the spectrum of the microearthquake catalog (formed by treating the catalog as a point process [e.g., *Brillinger*, 1974]). The catalog spectrum does not provide evidence for cyclicity at tidal periods, and cross-spectral analysis with concurrently measured deep-sea tide gauge data (i.e., ocean tides) and predicted solid earth tides do not yield statistically significant coherencies (Figure 4).

We restrict our analyses to the best located events, which we define as those events with RMS errors ≤ 20 ms. Seismic moments for these 6207 (of 32,078 total) micro-earthquakes, estimated from spectral

Figure 6. Waveforms and spectra of three microearthquake events. Event waveforms are from vertical channels of the five OBSs and have different velocity scales to better convey the diversity of waveforms across the network. Event power spectral density, which is calculated using the multitaper method with NW = 4, is shown for each waveform. Events have single-phase arrivals and very different waveforms across the network suggestive of nondouble couple sources whose paths are affected by local scattering. See Figure 8 for estimated hypocenters (labeled EX1, EX2, and EX3).

levels between 5 and 50 Hz [*Pearson*, 1982; *Deichmann*, 2006], fall between 10^{13} and 10^{16} dyn cm, corresponding to local magnitudes of $-1.4 \leq M_L \leq 0.5$, with an average of -0.95 and a median of -0.99 (Figure 5). The skew of the histogram toward larger magnitude events is presumably because the smallest events go undetected. The total moment release for these events over the 9 month deployment is $10^{18.6}$ dyn cm, which is equivalent to a single event with a local magnitude of $M_L \sim 1.7$. For comparison, the 19,232 microearthquakes associated with detachment faulting and tectonic extension at the TAG segment over the same time period had local magnitudes ranging from $1 \leq M_L \leq 4$ to a total moment release of $10^{21.3}$ dyn cm [*deMartin et al.*, 2007]. These results demonstrate that although the seismicity rate within the active TAG deposit is high, the total energy budget of these very small microearthquakes is negligible compared to that of tectonic extension along the segment.

Figure 7. Histogram of hypocentral RMS error for events with errors < 200 ms. Only those events with hypocentral errors < 20 ms (black bars) are used to examine spatial patterns in Figures 8 and 9.
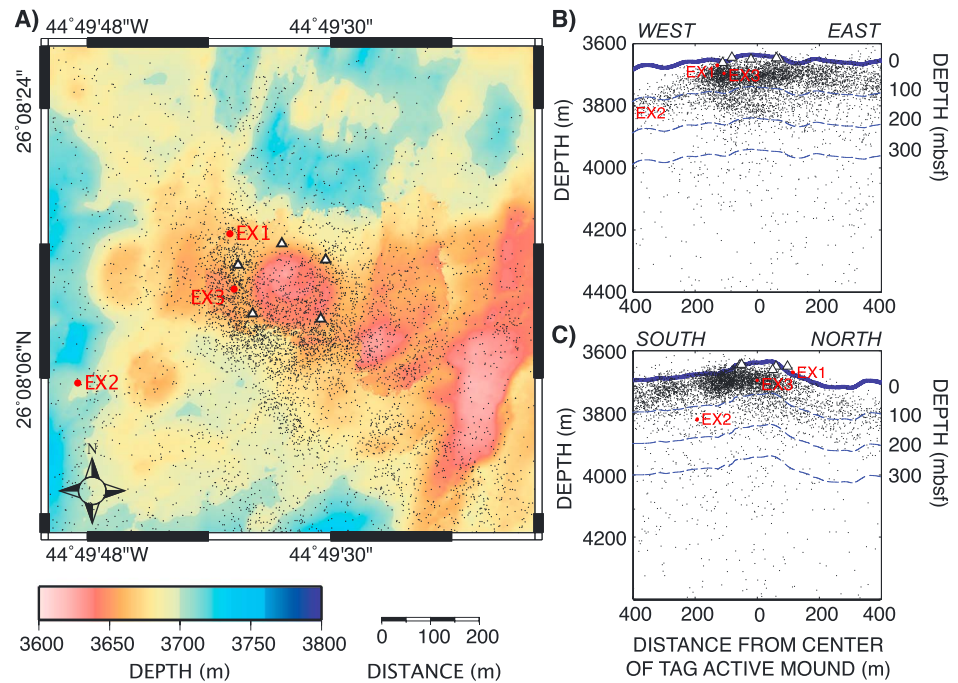
3.1. Microearthquake Characteristics and Hypocenters

The microearthquake seismograms are characterized by impulsive, short-period (15–30 Hz), *P* wave arrivals with durations of <1 s (Figure 6). *S* arrivals are not generally observed in the seismograms, although near-field effects combined with the 100 Hz sampling rate may confound identification of secondary arrivals. The small size of the earthquakes and poor signal-to-noise ratio makes it difficult to accurately determine the robust polarity observations of first arrivals, and this, combined with the small number of stations available for analysis, precludes the estimation of reliable focal plane solutions.
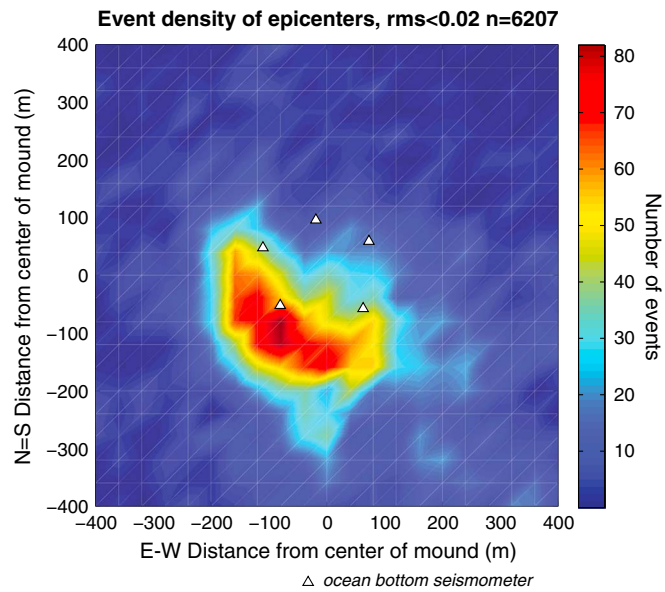
We cross-correlated waveforms for 5000 randomly selected events with the next 100 events in time and 100 additional random events from the catalog to assess waveform similarity. We found that less than 1% of the catalog is correlated above a threshold of $r^2 \geq 0.7$, such that it was not possible to use relative relocation nor stacking methods to refine our hypocentral and arrival polarity estimates. Because of the low signal-to-noise ratios and potential near-field propagation effects, it is difficult to rule out the possibility of repeating sources, but the observed lack of waveform similarity is likely at least partly due to high levels of scattering in the heterogeneous deposit, as discussed below.

Hypocenters for the 6207 events with RMS errors < 20 ms exhibit considerable scatter, but it is clear that the most intense activity occurs within the upper ~200 m of crust to the south and west of the mound periphery

Figure 8. (a) Epicenters of 6207 events with location errors < 20 ms. Average 1σ confidence ellipses have axis diameters in the *x* and *y* directions of approximately +/−200m. (b) East-west depth section (no vertical exaggeration). (c) North-south depth section (no vertical exaggeration). Average 1σ confidence limits in the vertical direction is ~187 m. Dashed blue lines in Figures 8b and Figure 8c demarcate depths in meters below the seafloor (meters below seafloor). Locations of example events from Figure 6 are shown in red.

Figure 9. A density map of 6207 epicenters serves to highlight the zone of densest seismicity on the south and west flanks of the mound.

(Figures 8 and 9). Much of the scatter in the hypocenter locations results from the combination of picking errors owing to the low signal-to-noise ratio of most arrivals and the fact that hypocenters are estimated with only 4 or 5 degrees of freedom (i.e., arrival time picks). The 6207 hypocenters with RMS errors < 20 ms have average 1σ confidence ellipses with axis diameters of 214 m, 202 m, and 187 m in the north–south, east–west, and vertical directions, respectively, which is large relative to the network aperture [*Wilcock and Toomey*, 1991]. The large, average, absolute errors reflect the fact that (1) the hypocenters (4 DOF) are located with four or five phase arrivals, and (2) the picking errors are large relative to the total travel time of the arrivals. As described above, we cannot exploit relative relocation methods based on waveform similarity to refine our hypocentral estimates, but the large number of events in the catalog allows us to discern some basic patterns. The highest density of hypocenters is found to the south and west of the mound at a depth of ~125 m below seafloor (Figure 9).

4. Discussion

Deploying a small-aperture (~200 m) network of five OBSs around the perimeter of the TAG active mound allowed us to detect ~32,000 and locate ~6200 very small ($M_L \sim -1$) microearthquakes within the zone of subsurface mineral deposition. We do not have enough data to formally constrain the focal mechanisms of these events, but the apparent lack of S arrivals and extremely short event durations (< 1 s) suggest a nondouble couple (i.e., volume change) as opposed to a shear failure source mechanism. Nondouble couple, flow-induced microearthquakes have been observed in geothermal areas [e.g., *Ross et al.*, 1996; *Miller et al.*, 1998; *Foulger et al.*, 2004] and hydraulic fracturing experiments [e.g., *Aki et al.*, 1982; *Cuenot et al.*, 2006; *Julian et al.*, 2007; *Šílený et al.*, 2009] on land, but this is the first time that a seismic network small enough to detect and locate such events has been deployed at a deep-sea hydrothermal field.

S arrivals in the seismograms may be obscured by near-field effects because the P arrival wavelengths (100–150 m) are comparable to the hypocentral distances for many events. Near-field effects complicate interpretation of seismograms [*Aki and Richards*, 2002; *Lokmer and Bean*, 2010; *Mangriotis et al.*, 2011], and it is conceivable that our inability to identify S arrivals stems at least partly from the fact that these phases have not fully separated from the P arrivals within the near field. The nominal arrival time difference between P and S waves from an event at 50–100 m depth beneath the mound to the seismic network is on the order of 30–60 ms, which corresponds to 3–6 samples at our sampling rate of 100 Hz. This indicates that S arrivals in the seismograms would most likely be found within the coda of the preceding P arrival and that the sampling rate employed in this study is too slow to allow for a rigorous distinction between P wave and S wave arrival times for many events in the catalog. However, although it may be difficult to determine the arrival time of an S wave, it should still be observable in the seismogram owing to differences in frequency content. Some of the seismograms in our data set could be interpreted this way (~10.2%), but many (~89.8%) of them do not exhibit the change in frequency content with time as is expected for traces with distinct P and S arrivals. We conclude that many, though perhaps not all, of the events lack an S phase, and we acknowledge that a denser seismic network sampling at rates on the order of 1 kHz will be required to properly image the seismograms and unequivocally constrain the source mechanisms.

PONTBRIAND AND SOHN
829

The near-field term decays as $1/r^2$ to a distance of half the P wavelength (~25–75 m) from the source and $1/r^3$ beyond that with distance (r) from the source [*Lokmer and Bean*, 2010]. Thus, near-field disturbance cannot explain the lack of S arrivals in our data, because most event hypocenters lie outside of the network and are more than a wavelength from at least some stations in the network. Filtering may be used to suppress near-field effects in homogeneous media, but in heterogeneous media it can only be accounted for with full three-dimensional modeling or full waveform inversion of the seismic wavefield [*Lokmer and Bean*, 2010; *Li et al.*, 2011]. A detailed three-dimensional seismic velocity model for the TAG active mound will therefore be required to accurately model the effects of near-field propagation on the seismograms.

The dissimilarity between seismograms from different stations for the same event, despite the small network aperture, is striking. This is partly attributable to coupling effects—for example, the spectral plots in Figure 6 show that STIR-13 has a coupling resonance at ~15 Hz—but much of the waveform dissimilarity is likely caused by scattering. Drill cores have shown that the TAG deposit is structurally heterogeneous over a range of length scales, and these heterogeneities likely result in considerable scatter of the seismic wavefield. Seismograms from a small-aperture network deployed at the Old Faithful geyser in Yellowstone National Park also exhibited a strong degree of dissimilarity, leading to the same conclusion [e.g., *Kieffer*, 1984; *Kedar et al.*, 1998]. More recent analyses of the Old Faithful seismic data have demonstrated that ambient noise/matched-field processing techniques may be used to image subsurface velocity heterogeneities with a sufficiently dense instrument network [*Cros et al.*, 2011], which presents an intriguing possibility for TAG and other deep-sea hydrothermal fields.

4.1. Potential Source Mechanisms

We do not have enough data to formally constrain the focal mechanisms, but we can assess the compatibility of the microearthquake data with a range of potential source mechanisms to identify plausible scenarios. Although the hanging wall hosting the active mound is clearly tectonized and extended [e.g., *Kleinrock and Humphris*, 1996], the monochromatic, single-phase (P wave) seismograms and the clustering at shallow depths within the deposit are inconsistent with a tectonic source mechanism. Tectonic sources should generate observable S arrivals, and models of seismic coupling indicate that the weak and unconsolidated rocks comprising the uppermost portion of the extrusive volcanic layer should slip stably (i.e., brittle creep) rather than seismogenically [e.g., *Cowie et al.*, 1998]. These considerations lead us to conclude that tectonic extension does not provide a plausible explanation for the majority of events in our data set. We also note that we do not observe any space-time correlation between the events observed at the active hydrothermal mound with the larger-scale seismicity associated with tectonic extension on the active detachment fault [*deMartin et al.*, 2007].

Thermal contraction in a deep-sea hydrothermal system occurs in places where hot rock is being cooled by cold seawater, and this may generate small microearthquakes [e.g., *Sohn et al.*, 2004]. However, the water-rock reaction zone where hot rock is cooled by hydrothermal fluids at TAG is somewhere at or below the detachment footwall interface (i.e., depths > 1.5 km below the seafloor), not in the upper 200 m of crust. The only plausible way to generate sustained rates of thermal contraction events in the shallow crust is by cooling a magmatic intrusion. For example, very small ($M_L \sim -1$) microearthquakes with purely P wave arrivals were observed by seismometers on the Kilauea Iki lava lake as it cooled in 1976 [*Chouet*, 1979], and these events bear some resemblance to our data. However, the presence of a magma body in the shallow crust is precluded by the results of an active source seismic refraction study conducted during the STAG experiment [*Canales et al.*, 2007]. The microearthquakes we observed are therefore not associated with thermal contraction of the deposit, which is likely maintained at a relatively stable thermal state during periods of prolonged discharge. We note, however, that there is a considerable amount of heat being conductively transferred within the deposit from high-temperature fluids rising from depth to cold pore fluids in the secondary circulation system [*Teagle et al.*, 1998; *Lowell et al.*, 2003]. This heat transfer may play a role in reaction-driven seismogenesis, as we discuss below.

Hydrothermal processes can generate nondouble couple events via hydraulic fracturing and vibrating fluids/bubbles [e.g., *Ross et al.*, 1996; *Miller et al.*, 1998; *Foulger et al.*, 2004]. Hydraulic fracturing can occur when fluid pressure exceeds the strength of the local host rock. The maximum fluid pressures that can be achieved in a hydrothermal system are constrained to be less than or equal to the buoyancy pressure, which is the

difference between the pressure at the base of the recharge and discharge limbs of the convection cell [*Cann and Strens*, 1989]. The buoyancy pressure (ΔP) in a convection cell with depth, z, is given by
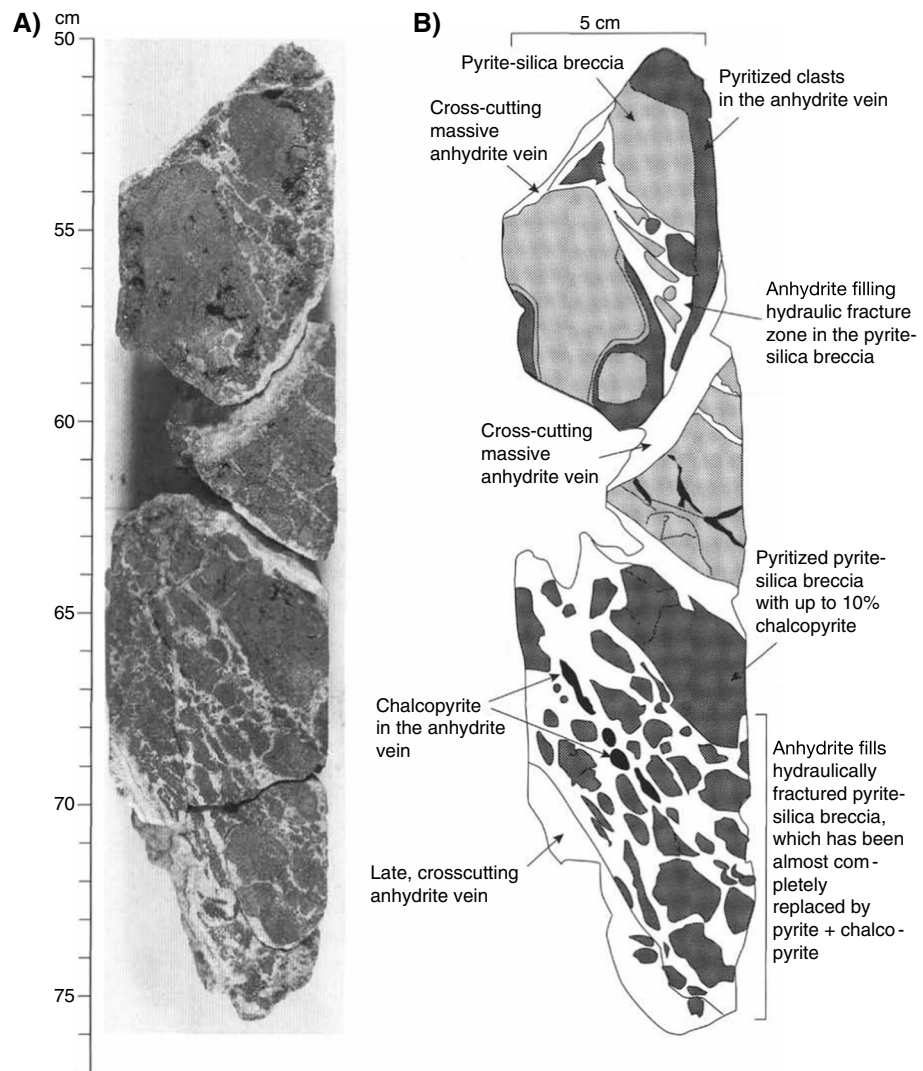
$$\Delta P = gz(\rho_{sw} - \rho_{ht}) \tag{1}$$

where g is gravitational acceleration, ρ_{sw} is the density of downgoing cold seawater, and ρ_{ht} is the density of rising hydrothermal fluid. The depth of convection in the primary circulation system is unknown, but based on geophysical evidence, values of 1.5 to 8 km below the seafloor are possible [*Canales et al.*, 2007; *deMartin et al.*, 2007]. Assuming a maximum temperature of 400°C for the rising fluids [e.g., *Violay et al.*, 2012], which corresponds to a fluid density of 663–800 kg m^{-3} [*Bischoff and Rosenbauer*, 1985; *Palliser and McKibben*, 1998], the buoyancy pressure in the primary circulation system is between ~5 and 18 MPa. Although the fracture strength of the matrix hosting flow at shallow depths in the deposit is not known, it is likely on the order of the confining pressure, which is ~39 MPa at a nominal depth of 125 m bsf, which is several times higher than the maximum buoyancy pressure.

In addition, the majority of the microearthquakes appear to occur off the periphery of the mound where there is no evidence for high-temperature discharge. Visual observations of black smoker (i.e., high-temperature) venting from Deep Submergence Vehicle *Alvin* and remotely operated vehicle *Jason 2* during the STAG experiment were restricted to the upper terrace of the TAG mound [*Sohn*, 2007a], which is consistent with high-temperature discharge being restricted to the central "core" of the hydrothermal system, rather than the peripheral region where the microearthquakes were observed. The peripheral region is believed to host a secondary circulation system that entrains cold seawater at shallow depths to cool the deposit [*Humphris et al.*, 1995; *Becker et al.*, 1996; *Honnorez et al.*, 1998]. Buoyancy pressures in the secondary circulation system are much less than those in the primary circulation system, because the convection cell is shallower and maximum fluid temperatures are ~400°C [*Alt and Teagle*, 1998]. Assuming that secondary circulation penetrates to a depth of 200 m (i.e., approximate base of seismogenic zone) and achieves maximum temperatures of 400°C ($\rho_{ht} = 579$ kg m^{-3}, [*Bischoff and Rosenbauer*, 1985; *Seyfried*, 1987]) the maximum buoyancy pressure is 0.88 MPa, which is considerably less than both the confining (~39 MPa) and differential (~2.6 MPa) pressures at the depth horizon of the microearthquakes (~125 m bsf). These calculations demonstrate that buoyancy pressures in both the primary circulation system associated with high-temperature discharge beneath the center of the mound, and the secondary circulation system presumed to operate off the mound periphery where the microearthquakes are predominantly located, are too small to generate high rates of hydraulic fracturing events beneath the mound. The volume of decompressing fluid required to produce an average magnitude event if hydraulic fracturing occurred with a stress drop equal to the maximum buoyancy pressure in the secondary recharge system is on the order of 10^4 m^3 [e.g., *Sohn et al.*, 1995]. As a result, we conclude that hydraulic fracturing is not a plausible source mechanism for the observed microearthquakes.

Collapsing bubbles and vibrating fluids are potential sources of hydrothermal microearthquakes and/or noise [*Kieffer*, 1984; *Kedar et al.*, 1996, 1998; *Vandemeulebrouck et al.*, 2010], but they are typically observed in subaerial systems where there are large density changes associated with the phase transition from liquid to gas [*Kieffer and Delany*, 1979]. The TAG active mound is located at a depth of 3670 m where ambient pressures are supercritical (critical pressure in the ocean corresponds to depths of ~3000 m), and the volume change associated with the transition from a fluid to a supercritical vapor is ~500 times smaller at these conditions compared to a subaerial geothermal field [e.g., *Driesner*, 2007]. In addition, the frequency content of a bubble collapse event is controlled to first order by the size (radius) of the bubble, the fluid density, and the ambient pressure [*Rayleigh*, 1917]. For idealized Rayleigh collapse at the ambient pressure of the TAG mound, a bubble radius on the order of 10 m would be required to generate the 20–40 Hz signals we observed, which is clearly unrealistic. Finally, none of the TAG exit fluid samples acquired/analyzed to date is saturated in dissolved gases (e.g., CO_2, H_2) [*Charlou et al.*, 1996]. These pieces of evidence argue strongly against bubble collapse and vibrating fluids as source mechanisms for the microearthquakes we observed.

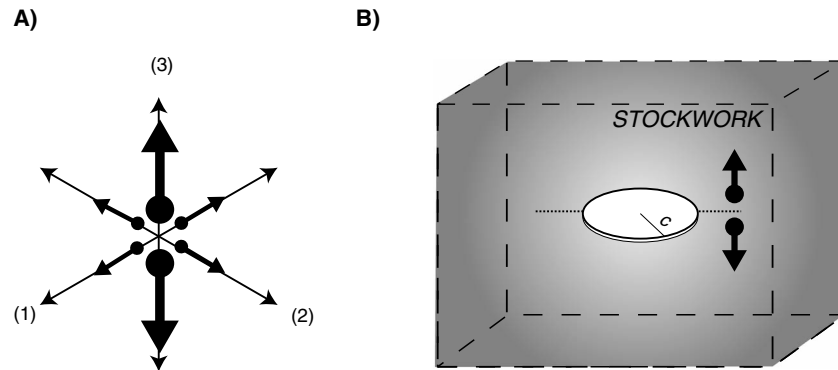### 4.2. Reaction-Driven Cracking

Reaction-driven cracking is a process that fractures the matrix hosting fluid flow as minerals are precipitated in pore spaces. The solid volume of a hydrothermal deposit increases as minerals are deposited in veins and pores, and this process (also known as "frost heave" and "salt weathering" in the literature) can generate large

Figure 10. (a) A photograph and (b) sketch of a section from ODP Leg 158, Hole 975C [*Humphris et al.*, 1996, Figure 16]. Hole 975C was drilled in the upper terrace of the mound ∼20 m southeast of the black smoker complex, and the section corresponds to a depth of ∼33 m bsf.

stresses capable of fracturing the host matrix [*Walder and Hallet*, 1985; *Scherer*, 1999, 2004; *Steiger*, 2005a, 2005b]. Cores recovered from the TAG active mound during ODP Leg 158 revealed a brecciated stockwork with an abundance of anhydrite veins, many of which contain textural evidence for fracturing. Anhydrite is a retrograde soluble mineral that precipitates from seawater when temperatures rise above 150°C through conductive heating or convective mixing with hydrothermal fluid and dissolves at cooler temperatures [*Edmond et al.*, 1995; *Chiba et al.*, 1998; *Teagle et al.*, 1998; *Lowell and Yao*, 2002; *Noiriel et al.*, 2010]. Anhydrite veins in the ODP cores fill complex, multistage fractures up to 45 cm in width [*Humphris et al.*, 1996], with textures typical of open-space filling. Individual growth bands reflect sequential precipitation within cavities and repeated opening of fractures. Some anhydrite veins contain angular clasts of competent, low-porosity wall rock, indicative of fracturing (Figure 10). In samples with multiple veins, the host rock is commonly shattered and healed by late anhydrite [*Humphris et al.*, 1996]. Textures of late anhydrite veining show that cementation and fracturing is a continual process during hydrothermally active periods. Anhydrite was recovered on broken clast surfaces and in veins and vugs throughout the stockworks, indicating that cold seawater penetrates to depths of at least 120 m bsf [*Humphris, Herzig et al.*, 1996].

The ODP cores demonstrate that anhydrite precipitation and fracturing of the basalt matrix occur concurrently within the same depth horizon as our microearthquakes, suggesting reaction-driven cracking as a

A)   B)

Figure 11. (a) Body force representation for mode I opening of a horizontal crack. (b) Schematic diagram of a horizontal, penny-shaped opening in the vertical direction.

plausible source mechanism. Anhydrite precipitation increases the solid volume of the deposit and can fracture the matrix by increasing normal stresses on vein surfaces. This process is self-sustaining because cracking maintains permeability and exposes fresh mineral surfaces in the fracture network, thereby creating a positive feedback between fluid flow and mineral precipitation.

To model the stresses generated by anhydrite precipitation at the TAG active mound we consider mode I tensile cracking of a penny-shaped fracture (Figure 11). There is no preferred orientation observed for the anhydrite veins observed in the drill cores [*Humphris et al.*, 1996], so to simplify the model we consider a horizontal crack opening under in-plane tension such that only the strain component Δe_{33} is nonzero (Figure 11a). We acknowledge that this is likely an oversimplified model for the source process (e.g., the impact of gravitational forces on the response of the medium to fracture is not considered, the cracks are not planar, etc.), but in the absence of more detailed information it provides a first-order assessment of the source properties required to generate a microearthquake of a given size. The moment density tensor of this source in an isotropic medium is

$$\boldsymbol{m} = \begin{pmatrix} \lambda\Delta e & 0 & 0 \\ 0 & \lambda\Delta e & 0 \\ 0 & 0 & (\lambda + 2\mu)\Delta e \end{pmatrix} \qquad (2)$$

where λ and μ are the Lamé parameters of the medium (Table 1). The moment tensor is found by integrating over the source volume, V,

$$\boldsymbol{M} = -V \begin{pmatrix} \lambda\Delta e & 0 & 0 \\ 0 & \lambda\Delta e & 0 \\ 0 & 0 & (\lambda + 2\mu)\Delta e \end{pmatrix} \qquad (3)$$

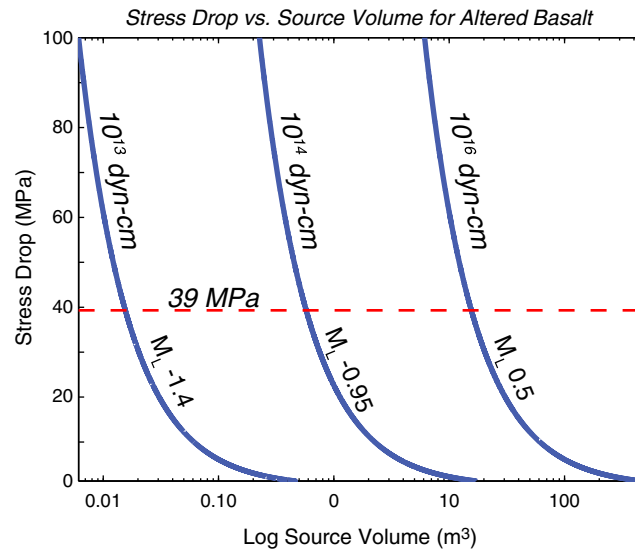where the source volume is modeled as a cylindrical (penny-shaped) vein with radius c and thickness L.

The scalar moment of this tensor is $M_0 = \frac{1}{\sqrt{3}}(\boldsymbol{M} : \boldsymbol{M})^{1/2}$, leading to,

$$M_0 = \frac{\Delta e V}{\sqrt{3}} \sqrt{2\lambda^2 + (\lambda + 2\mu)^2}. \qquad (4)$$

Table 1. Lamé Parameters and Young's Moduli Derived From Seismic Velocity and Bulk Density Measurements of Hand Core Samples of Altered Basalt Taken From TAG Active Mound Subsurface [*Ludwig et al.*, 1998]

Rock Type	Depth (meters below seafloor)	Lamé Parameter μ (GPa)	Lamé Parameter λ (GPa)	Young's Modulus E (GPa)	Core Section(s) 158–957
Altered basalt	42.91–46.67	30.42	41.81	78.45	M- 9R-1, 61–63 cm; 10R-1,
		30.42	44.23	78.86	39–41 cm; 10R-1, 47–49 cm
		33.49	35.67	84.25	
		33.49	38.09	84.80	
Nominal parameters		31.96	39.95		

Figure 12. The relationship between stress drop, source volume, and microearthquake size in our reaction-driven cracking model. The dashed red line indicates the confining pressure (39 MPa) at 125 m bsf.

Following the *Scholz* [2002] model for a penny-shaped crack, the relationship between stress drop and strain is

$$\Delta\sigma = \frac{7\pi}{16}\mu\Delta e \qquad (5)$$

We can substitute equation (5) into equation (4) to obtain the relationship between the seismic moment of a reaction-driven cracking event and the volume and stress drop of a penny-shaped source region,

$$V\Delta\sigma = \sqrt{3}M_0\frac{7\pi}{16}\mu\left[\sqrt{2\lambda^2 + (\lambda + 2\mu)^2}\right]^{-1}. \qquad (6)$$

We can use equation (6) to find the combinations of source volume and stress drop required to generate a microearthquake of a given size (Figure 12). The Lamé parameters for TAG mound basalts measured on hand samples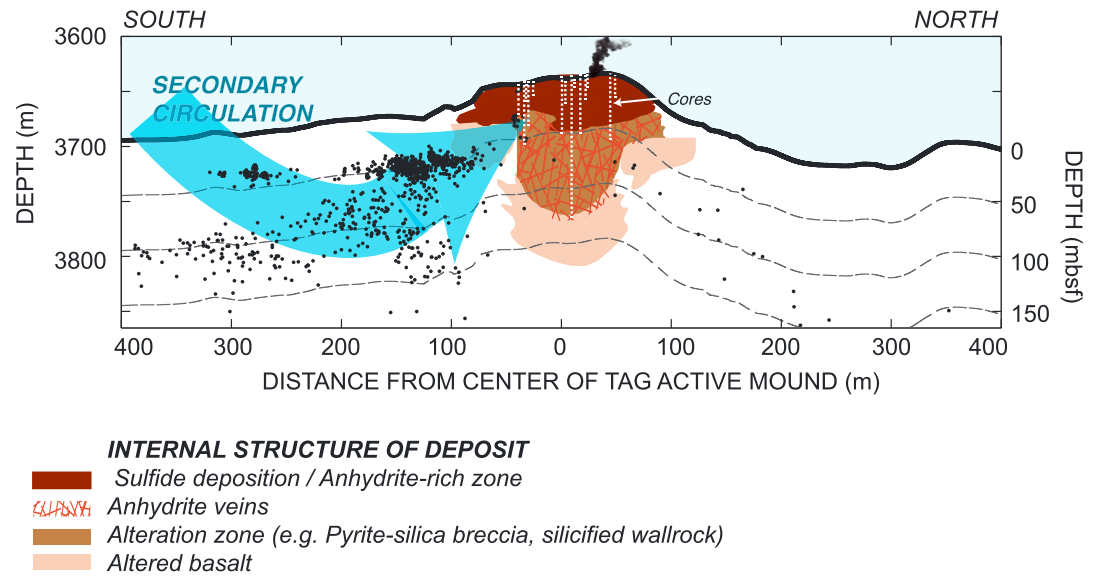 from the ODP drill cores are shown in Table 1, based on which we assign nominal values of $\mu = 39.95$ GPa, $\lambda = 31.96$ GPa. To assess compatibility with our observations, we set the target earthquake size equal to the "average" microearthquake in our catalog ($M_L = -0.95$, $M_o = 3.7 \times 10^{14}$ dyn cm). The stress drops of the microearthquakes are unknown, but we can consider a range of potential values. Published values in the earthquake seismology literature stretch from 0.1 to 100 MPa [e.g., *Abercrombie and Leary*, 1993; *Prejean and Ellsworth*, 2001; *Imanishi et al.*, 2004], and stress drops of up to 100 MPa have been observed in laboratory salt weathering experiments [*Steiger*, 2005a], such that 100 MPa appears to be a reasonable upper limit. At the lower limit, fracturing is unlikely to occur unless stresses exceed the confining stress (39 MPa for microearthquakes at 100 m bsf) or fracturing occurs along already-weakened rock.

The source volume required to generate an "average" microearthquake observed during our study (i.e., $M_0 = 3.7 \times 10^{14}$ dyn cm) under the limiting stress drop assumptions are listed in Table 2. We find that source volumes of ≥ 0.61 m^3 are sufficient if the stress drop is greater than or equal to the confining pressure. We can convert the source volume estimates into estimates for crack size by assuming that veins obey a linear fracture-length relationship, $L = C_1(2c)$, where L is the crack thickness, c is the crack radius, and $C_1 = 1.0 \times 10^{-3}$ is a geologically representative aspect ratio [*Vermilye and Scholz*, 1995]. Under this assumption the source radius can be written as $c = \sqrt[3]{V/2\pi C_1}$, yielding crack size (radius) values of 4.6 m and 3.4 m required to generate an average event from our catalog for stress drops equal to 39 MPa (confining stress) and 100 MPa, respectively (Table 2). Under our assumption for C_1 these cracks have thicknesses of 9.2 mm and 6.7 mm, respectively, which is somewhat larger than the median anhydrite vein thickness of 4 mm measured in the ODP cores [*Humphris et al.*, 1996, Table 5].

4.3. Implications for Anhydrite Precipitation

Our analysis indicates that reaction-driven cracking is a plausible mechanism for the small microearthquakes we observed beneath the TAG active mound. In this model the microearthquake hypocenters delineate zones of active anhydrite deposition (Figure 13), and the size of an individual event is directly related to an incremental volume of anhydrite deposited in the source region. The microearthquakes cluster along the

Table 2. Source Volume by Stress Drop Required to Generate a −0.95 Magnitude Microearthquake in Altered Basalt

Stress Drop	Source Volume (m^3)	Crack Radius (m)	Crack Thickness (mm)
100 MPa	0.24	3.36	6.7
Confining pressure 39 MPa	0.61	4.58	9.2
Differential pressure 2.6 MPa	8.99	11.27	22.5

Figure 13. A depth section of 1157 hypocenters located within a 100 m wide north-south plane through the center of the TAG active mound shows a seismogenic zone focused to the south of the deposit and < 150 m below the seafloor. Many hypocenters lie within the anhydrite-rich zone and anhydrite-veined alteration zones of the TAG active mound as inferred from ODP drill cores (white dashed lines) [*Humphris et al.*, 1995]. A well-defined horizontal band of seismicity that likely marks a zone of reaction-driven cracking where secondary circulation recharge fuels the most intense anhydrite deposition.

southwest corner of the active mound (Figure 8). This region is not covered by the fine-scale microbathymetric map generated during the STAG experiment [*Roman and Singh*, 2007], but the area may correspond to crosscutting fissures imaged by ARGO II cameras and mapped by *Bohnenstiehl and Kleinrock* [2000] (Figure 2). Within the hanging wall block, orientations of ~40% of fissures deviate significantly (> 45°) from those predicted by the regional tectonic stress field and small extensional fissures (several tens of meters in length and 0.7 m wide on average) crosscut the 100,000 year old crust (Figure 2) [*Kleinrock and Humphris*, 1996; *Bohnenstiehl and Kleinrock*, 2000]. First-order estimates indicate that these fissures are restricted to < 500 m depth with a mean value of 70 m [*Bohnenstiehl and Kleinrock*, 2000]. Fissure orientations to the southwest of the mound are consistent with the distribution of microearthquake hypocenters, suggesting that the hypocentral cloud represents fissures where anhydrite was being actively deposited.

We can estimate the volume of anhydrite precipitated during our experiment by summing the volume change associated with the microearthquakes. Under the confining stress and 100 MPa stress drop scenarios, a $M_L = -0.95$ ($M_0 = 3.7 \times 10^{14}$ dyn cm) microearthquake generates volume changes of 31 cm^3 and 58 cm^3, respectively. If we assume a seismicity rate of 243 microearthquakes per day (as observed at the beginning of the experiment before one of the instruments failed), then we obtain an annual volume change of between 27 m^3 and 51 m^3. The total volume of anhydrite within the active TAG deposit has been estimated to be 2×10^4 m^3 [*Tivey et al.*, 1998], such that in the absence of dissolution it would take between 391 and 727 years to precipitate all the anhydrite in the deposit based on our estimated rates.

If we assume that the microearthquakes occur as cold seawater is heated and anhydrite is precipitated in the secondary circulation system, then we can use these precipitation rate estimates to constrain fluid fluxes in the secondary system. We can express fluid flux as

$$r_{sw} = R_{anh}(r_{anh}V_{anh})^{-1}, \tag{7}$$

where R_{anh} is our estimated anhydrite deposition rate (27–51 m^3 y^{-1}), r_{anh} is the molar concentration of anhydrite in seawater (~0.0143 mol anhydrite per kilogram of fluid [*Tivey et al.*, 1998]), and V_{anh} is the molar volume of anhydrite (4.6×10^{-5} m^3 mol^{-1} [*Robie and Hemingway*, 1995]). Using these values, we obtain flux estimates of 4.1–7.7 × 10^7 kg y^{-1}, corresponding to rates of 1.3–2.5 kg s^{-1}, which are 1–2% of the ~100 kg s^{-1} estimated by *Hannington et al.* [1998] for high-temperature fluid flux at the TAG black smoker complex. Our flux estimates represent minimum values since not all entrained seawater may be heated to temperatures high enough for anhydrite precipitation.

We can also use our results to constrain the heat flux required to drive anhydrite deposition. Following *Tivey et al.* [1998], the heat flux (H) required for anhydrite deposition is given by

$$H = r_{sw}c_{sw}\Delta T, \tag{8}$$

where c_{sw} is the heat capacity of seawater (4100 J kg^{-1} K^{-1} at 400 bars [*Bischoff and Rosenbauer*, 1985]) and ΔT is the fluid temperature increase (required to heat cold seawater from ~2°C to anhydrite precipitation temperatures of ~160–350°C). Under our entrainment rate estimates of 1.3 to 2.5 kg s^{-1} the heat flux required to drive anhydrite deposition is 0.8 to 3.6 MW, which is less than 1% of the ~1 GW total heat flux estimated for the TAG active mound [*Wichers et al.*, 2005].

4.4. Implications of Reaction-Driven Microearthquakes for Circulation Patterns

Seismicity in our microearthquake catalog is concentrated to the south and west of the active mound. If our hypothesis that these events are triggered by reaction-driven cracking in response to anhydrite precipitation in the secondary circulation system is correct, then the hypocentral patterns indicate that the secondary circulation system is not symmetric about the mound but rather offset to the south and west. It is possible that uniform velocity assumptions influence the locations of the hypocenters and that a low-velocity, brecciated sulfide body in the center of the OBS network may move hypocenters closer to the network and the center of the sulfide deposit. Thus, we do not speculate regarding the cause of the asymmetry, but we note that conductive heat flow measurements made from 1993 to 1995 delineated a "coherent belt of very low heat flow ($<$ 20 mW m^2)" on the west side of the mound [*Becker et al.*, 1996]. These low heat flow measurements were taken as evidence for shallow recharge of cold bottom water, i.e., a recharge zone for secondary circulation, which is broadly consistent with our results, although the heat flow measurements were acquired on the mound proper rather than off the periphery where the microearthquake hypocenters are located. The black smoker complex is offset from center to the north of the deposit, and gravity profiles suggest that the thickness of the sulfide deposit decreases from north (~ 50 m thick) to south (~10 m thick) [*Evans*, 1996]. It is possible that the offset of the primary upflow zone and the nonuniform subsurface structure contribute to the asymmetry of secondary circulation, but models are needed to evaluate this idea.

A dense cluster of microearthquakes is focused in a narrow depth interval at ~125 m bsf, and there are essentially few events below this "lid" (Figure 8). This pattern implies that in the secondary circulation system, temperatures greater than 150°C (required for anhydrite precipitation) are reached by conductive heating or convective mixing with hydrothermal fluids at depths of ~125 m and that much of the anhydrite is immediately precipitated upon reaching this depth/temperature horizon. This result could prove useful for constraining circulation models at TAG, and it could also provide testable hypotheses for drilling.

We conclude by noting that the small number of stations employed in our study results in relatively large absolute hypocentral errors (i.e., scatter) that hinder interpretation of spatial patterns. Having demonstrated that a small-aperture OBS network is capable of detecting very small microearthquakes associated with fluid flow in a deep-sea hydrothermal deposit, the logical next step would be to deploy a denser OBS network with sampling rates of ~1 kHz to reduce hypocentral uncertainties and to allow for a more rigorous analysis of the seismograms and focal mechanism(s).

References

Abercrombie, R., and P. Leary (1993), Source parameters of small earthquakes recorded at 2.5 km depth, Cajon Pass, Southern California: Implications for earthquake scaling, *Geophys. Res. Lett.*, *20*(14), 1511–1514.

Aki, K., and P. G. Richards (2002), *Quantitative Seismology*, University Science Books, Sausalito, Calif.

Aki, K., M. Fehler, R. L. Aamodt, J. N. Albright, R. M. Potter, C. M. Pearson, and J. W. Tester (1982), Interpretation of seismic data from hydraulic fracturing experiments at the Fenton Hill, New Mexico, hot dry rock geothermal site, *J. Geophys. Res.*, *87*(B2), 936–944, doi:10.1029/JB087iB02p00936.

Alt, J. C., and A. H. Teagle (1998), Probing the TAG hydrothermal mound and stockwork: Oxygen-isotopic profiles from deep ocean drilling, in *Proceedings of the Ocean Drilling Program, Scientific Results*, vol. 158, edited by P. M. Herzig et al., pp. 85–90, Ocean Drilling Program, College Station, Tex.

Bame, D., and M. Fehler (1986), Observations of long period earthquakes accompanying hydraulic fracturing, *Geophys. Res. Lett.*, *13*(1), 149–152.

Becker, K., R. Von Herzen, J. Kirklin, R. Evans, D. Kadko, M. Kinoshita, O. Matsubayashi, R. Mills, A. Schultz, and P. Rona (1996), Conductive heat flow at the TAG active hydrothermal mound: Results from 1993–1995 submersible surveys, *Geophys. Res. Lett.*, *23*(23), 3463–3466.

Bianco, F., E. Del Pezzo, G. Saccorotti, and G. Ventura (2004), The role of hydrothermal fluids in triggering the July-August 2000 seismic swarm at Campi Flegrei, Italy: Evidence from seismological and mesostructural data, *J. Volcanol. Geotherm. Res.*, *133*, 229–246, doi:10.1016/S0377-0273(03)00400-1.

Bischoff, J. L., and R. J. Rosenbauer (1985), An empirical equation of state for hydrothermal seawater (3.2 percent NaCl), *Am. J. Sci.*, *285*, 725–763.

Bohnenstiehl, D. R., F. Waldhauser, and M. Tolstoy (2008), Frequency-magnitude distribution of microearthquakes beneath the 9°50′N region of the East Pacific Rise, October 2003 through April 2004, *Geochem. Geophys. Geosyst*, *9*, Q10T03, doi:10.1029/2008GC002128.

Bohnenstiehl, D. R., and M. C. Kleinrock (2000), Fissuring near the TAG active hydrothermal mound, 26°N on the Mid-Atlantic Ridge, *J. Volcanol. Geotherm. Res.*, *98*, 33–48.

Brillinger, D. R. (1974), Statistical inference for stationary point processes, in *Proceedings of the Summer Research Institute on Statistical Inference for Stochastic Processes*, vol. 1, pp. 55–99, Indiana Univ., Bloomington, Ind.

Campbell, A. C., et al. (1988), Chemistry of hot springs on the Mid-Atlantic Ridge, *Nature*, *335*(6), 514–519.

Canales, J. P., R. A. Sohn, and B. J. deMartin (2007), Crustal structure of the Trans-Atlantic Geotraverse (TAG) segment (Mid-Atlantic Ridge, 26°100N): Implications for the nature of hydrothermal circulation and detachment faulting at slow spreading ridges, *Geochem. Geophys. Geosyst.*, *8*, Q08004, doi:10.1029/2007GC001629.

Cann, J. R., and M. R. Strens (1989), Modeling periodic megaplume emission by black smoker systems, *J. Geophys. Res.*, *94*(B9), 12,227–12,237.

Charlou, J. L., J. P. Donval, P. Jean-Baptiste, A. Dapoigny, and P. A. Rona (1996), Gases and helium isotopes in high temperature solutions sampled before and after ODP Leg 158 drilling at TAG hydrothermal field (26°N, MAR), *Geophys. Res. Lett.*, *23*(23), 3491–3494.

Chiba, H., N. Uchiyama, and D. A. H. Teagle (1998), Stable isotope study of anhydrite and sulfide minerals at the TAG hydrothermal mound, Mid-Atlantic Ridge, 26°N, in *Proceedings of the Ocean Drilling Program, Scientific Results*, vol. 158, edited by P. M. Herzig et al., pp. 85–90, Ocean Drilling Program, College Station, Tex.

Chouet, B. (1979), Sources of seismic events in the cooling lava lake of Kilauea Iki, Hawaii, *J. Geophys. Res.*, *84*(B5), 2315, doi:10.1029/JB084iB05p02315.

Copley, J. T. P., P. A. Tyler, C. L. Van Dover, A. Schultz, P. Dickson, S. Singh, and M. Sulanowska (1999), Subannual temporal variation in faunal distributions at the TAG hydrothermal mound (26°N, Mid-Atlantic Ridge), *Mar. Ecol.*, *20*(3–4), 291–306.

Cros, E., P. Roux, J. Vandemeulebrouck, and S. Kedar (2011), Locating hydrothermal acoustic sources at Old Faithful Geyser using Matched Field Processing, *Geophys. J. Int.*, *187*(1), 385–393, doi:10.1111/j.1365-246X.2011.05147.x.

Cuenot, N., J. Charlety, L. Dorbath, and H. Haessler (2006), Faulting mechanisms and stress regime at the European HDR site of Soultz-sous-Forets, France, *Geothermics*, *35*, 561–575, doi:10.1016/j.geothermics.2006.11.007.

Deichmann, N. (2006), Local magnitude, a moment revisited, *Bull. Seismol. Soc. Am.*, *96*(4A), 1267–1277, doi:10.1785/0120050115.

deMartin, B. J., R. A. Sohn, J. P. Canales, and S. E. Humphris (2007), Kinematics and geometry of active detachment faulting beneath the Trans-Atlantic Geotraverse (TAG) hydrothermal field on the Mid-Atlantic Ridge, *Geology*, *35*, 711–714.

Driesner, T. (2007), The system H2O-NaCl, Part II: Correlations for molar volume, enthalpy, and isobaric heat capacity from 0 to 1000_C, 1 to 5000 bar, and 0 to 1 XNaCl, *Geochim. Cosmochim. Acta*, *71*, 4902–4919, doi:10.1016/j.gca.2007.05.026.

Edmond, J. M., A. C. Campbell, M. R. Palmer, G. P. Klinkhammer, C. R. German, H. N. Edmonds, H. Elderfield, G. Thompson, and P. A. Rona (1995), Time series studies of vent fluids from the TAG and MARK sites (1986, 1990) Mid-Atlantic Ridge: A new solution chemistry model and mechanism for Cu/Zn zonation in massive sulfide orebodies, in *Hydrothermal Vents and Processes*, vol. 87, edited by L. M. Parson, C. L. Walker, and D. R. Dixon, pp. 77–86, Geological Society of London Special Publication, London, U.K.

Evans, R. L. (1996), A seafloor gravity profile across the TAG hydrothermal mound, *Geophys. Res. Lett.*, *23*(23), 3447–3450.

Ferrazzini, V., B. Chouet, M. Fehler, and K. Aki (1990), Quantitative analysis of long-period events recorded during hydrofracture experiments at Fenton Hill, New Mexico, *J. Geophys. Res.*, *95*(B13), 21,871, doi:10.1029/JB095iB13p21871.

Foreman, M. G. G. (1977), Manual for tidal heights analysis and prediction, Pacific Marine Science Report 77–10, Institute of Ocean Sciences, Patricia Bay, Victoria, B.C.

Foulger, G. R., B. R. Julian, D. P. Hill, A. M. Pitt, P. E. Malin, and E. Shalev (2004), Non-double-couple microearthquakes at Long Valley Caldera, California, provide evidence for hydraulic fracturing, *J. Volcanol. Geotherm. Res.*, *132*, 45–71, doi:10.1016/S0377-0273(03)00420-7.

Galkin, S. V., and L. I. Moskalev (1990), Hydrothermal fauna of the Mid-Atlantic Ridge, *Okeanologica*, *30*, 842–847.

Hannington, M. D., A. G. Galley, P. M. Herzig, and S. Petersen (1998), Comparison of the TAG mound and stockwork complex with Cyprus-type massive sulfide deposits, in *Proceedings of the Ocean Drilling Program, Scientific Results*, vol. 158, edited by P. M. Herzig et al., pp. 231–254, Ocean Drilling Program, College Station, Tex.

Herzig, P. M., S. E. Humphris, D. J. Millerand, and R. A. Zierenberg (1998a), *Proceedings of the Ocean Drilling Program, Scientific Results*, vol. 158, Ocean Drilling Program, College Station, Tex.

Herzig, P. M., S. Petersen, and M. D. Hannington (1998b), Geochemistry and sulfur isotopic composition of the TAG hydrothermal mound, Mid-Atlantic Ridge, 26°N, in *Proceedings of the Ocean Drilling Program, Scientific Results*, vol. 158, edited by P. M. Herzig et al., pp. 47–40, Ocean Drilling Program, College Station, Tex.

Honnorez, J. J., J. C. Alt, and S. E. Humphris (1998), Vivisection and autopsy of active and fossil hydrothermal alterations of basalt beneath and within the TAG hydrothermal mound, in *Proceedings of the Ocean Drilling Program, Scientific Results*, vol. 158, edited by P. M. Herzig et al., pp. 231–254, Ocean Drilling Program, College Station, Tex.

Humphris, H., et al. (1996), TAG: Drilling an active hydrothermal system on a sediment-free slow-spreading ridge, Proceedings of the Ocean Drilling Program, Initial Reports, vol. 158, Ocean Drilling Program, College Station, Tex.

Humphris, S., et al. (1996), TAG-1 Area, in *Proceedings of the Ocean Drilling Project, Initial Reports*, vol. 158, edited by S. E. Humphris et al., pp. 65–140, Ocean Drilling Program, College Station, Tex.

Humphris, S. E., et al. (1995), The internal structure of an active sea-floor massive sulphide deposit, *Nature, 377*, 713–716.

Humphris, S. E., and M. C. Kleinrock (1996), Detailed morphology of the TAG active hydrothermal mound: Insights into its formation and growth, *Geophys. Res. Lett.*, *23*(23), 3443–3446.

Humphris, S. E., and M. K. Tivey (2000), A sysnthesis of geological and geochemical investigations of the TAG hydrothermal field: Insights into fluid-flow and mixing processes in a hydrothermal system, *Geol. Soc. Am. Spec. Pap.*, *349*, 213–235.

Humphris, S. E., and J. R. Cann (2000), Constraints on the energy and chemical balances of the modern TAG and ancient Cyprus seafloor sulfide deposits, *J. Geophys. Res.*, *105*(B12), 28,477–28,488.

Humphris, S. E., and W. Bach (2005), On the Sr isotope and REE compositions of anhydrites form the TAG seafloor hydrothermal system, *Geochim. Cosmochim. Acta*, *69*(6), 1511–1525, doi:10.1016/j.gca.2004.10.004.

Imanishi, K., W. L. Ellsworth, and S. G. Prejean (2004), Earthquake source parameters determined by the SAFOD Pilot Hole seismic array, *Geophys. Res. Lett.*, *31*, L12S09, doi:10.1029/2004GL019420.

Julian, B. R., G. R. Foulger, and F. Monastero (2007), Microearthquake moment tensors from the Coso Geothermal area, in *Proceedings, Thirty-Second Workshop on Geothermal Reservoir Engineering*, Paper SGP-TR-183, Stanford Univ., Stanford, Calif.

Kagan, Y. Y., and D. D. Jackson (1991), Long-term earthquake clustering, *Geophys. J. Int.*, *104*, 117–133.

Karson, J. A., and P. A. Rona (1990), Block-tilting, transfer faults, and structural control of magmatics and hydrothermal processes in the TAG area, Mid-Atlantic Ridge 26°N, *Geol. Soc. Am. Bull.*, *102*, 1635–1645.

Kedar, S., B. Sturtevant, and H. Kanamori (1996), The origin of harmonic tremor at Old Faithful geyser, *Nature, 379,* 708–711.

Kedar, S., H. Kanamori, and B. Sturtevant (1998), Bubble collapse as the source of tremor at Old Faithful Geyser, *J. Geophys. Res., 103*(B10), 24,283–24,299.

Kieffer, S. W. (1984), Seismicity at Old Faithful Geyser: An isolated source of geothermal noise and possible analogue of volcanic seismicity, *J. Volcanol. Geotherm. Res., 22,* 59–95.

Kieffer, S. W., and J. M. Delany (1979), Isentropic decompression of fluids from crustal and mantle pressures, *J. Geophys. Res., 84*(B4), 1611, doi:10.1029/JB084iB04P01611.

Kleinrock, M. C., and S. E. Humphris (1996), Structural control on seafloor hydrothermal activity at the TAG active mound, *Nature, 382,* 149–153.

Lalou, C., G. Thompson, M. Arnold, E. Brichet, E. Druffel, and P. A. Rona (1990), Geochronology of TAG and Snake Pit hydrothermal fields Mid-Atlantic Ridge: Witness to a long and complex hydrothermal history, *Earth Planet. Sci. Lett., 97,* 113–128.

Lalou, C., J. L. Reyss, E. Brichet, M. Arnold, G. Thompson, Y. Fouquet, and P. A. Rona (1993), New age data for Mid-Atlantic Ridge hydrothermal sites: TAG and Snakepit geochronology revisited, *J. Geophys. Res., 98*(B6), 9705–9713.

Lalou, C., J. L. Reyss, and E. Brichet (1998), Age of sub-bottom sulfide samples at the TAG active mound, in *Proceedings of the Ocean Drilling Program, Scientific Results,* vol. 158, edited by P. M. Herzig et al., pp. 111–117, Ocean Drilling Program, College Station, Tex.

Li, J., H. Zhang, H. Sadi Kuleli, and M. N. Toksoz (2011), Focal mechanism determination using high-frequency waveform matching and it sapplication to small magnitude induced earthquakes, *Geophys. J. Int., 184,* 1261–1274.

Lokmer, I., and C. J. Bean (2010), Properties of the near-field term and its effect on polarization analysis and source locations of long-period (LP) and very-long-period (VLP) seismic events at volcanoes, *J. Volcanol. Geotherm. Res., 192,* 35–47, doi:10.1016/j.jvolgeores.2010.02.008.

Lowell, R. P., and Y. Yao (2002), Anhydrite precipitation and the extent of hydrothermal recharge zones at ocean ridge crests, *J. Geophys. Res., 107*(B9), 2182, doi:10.1029/2001JB001289.

Lowell, R. P., Yao, Y., and L. N. Germanovich (2003), Anhydrite precipitation and the relationship between focused and diffuse flow in seafloor hydrothermal systems, *J. Geophys. Res., 108*(B9), 2424, doi:10.1029/2002JB002371.

Ludwig, R. J., G. J. Iturrino, and P. A. Rona (1998), 23. Seismic velocity-porosity relationship of sulfide, sulfate, and basalt samples from the TAG hydrothermal mound, in *Proceedings of the Ocean Drilling Program, Scientific Results,* vol. 158, edited by P. M. Herzig et al., pp. 313–328, Ocean Drilling Program, College Station, Tex.

Mangriotis, M.-D., J. W. Rector III, and E. F. Herkenhoff (2011), Effects of the near-field on shallow seismic studies, *Geophysics, 76*(1), B9–B18, doi:10.1190/1,3517512.

Matsumoto, K., T. Sato, T. Takanezawa, and M. Ooe (2001), GOTIC2: A program for computation of oceanic tidal loading effect, *J. Geodetic Soc. Jpn., 47*(1), 243–248.

McDonald, M. A., J. A. Hildebrand, and S. C. Webb (1995), Blue and fin whales observed on a seafloor array in the Northeast Pacific, *J. Acoust. Soc. Am., 98*(2), 712–721.

Miller, A. D., G. R. Foulger, and B. R. Julian (1998), Non-double-couple earthquakes: 2 Observations, *Rev. Geophys., 36*(4), 551–568.

Mills, R. A., D. A. H. Teagle, and M. K. Tivey (1998), Fluid mixing and anhydrite precipitation within the TAG mound, in *Proceedings of the Ocean Drilling Program, Scientific Results,* vol. 158, edited by P. M. Herzig et al., pp. 119–127, Ocean Drilling Program, College Station, Tex.

Noiriel, C., F. Renard, M.-L. Doan, and J.-P. Gratier (2010), Intense fracturing and fracture sealing induced by mineral growth in porous rocks, *Chem. Geol., 269,* 197–209, doi:10.1016/j.chemgeo.2009.09.018.

Palliser, C., and R. McKibben (1998), A model for deep geothermal brines, II: Thermodynamic properties – Density, *Transp. Porous Media, 33,* 129–154.

Pearson, C. (1982), Parameters and a magnitude moment relationship from small earthquakes obseruved during hydraulic fracturing experiments in crystalline rocks, *Geophys. Res. Lett., 9*(4), 404–407.

Percival, D. B., and A. T. Walden (1993), *Spectral Analysis for Physical Applications: Multitaper and Conventional Univariate Techniques,* Cambridge Univ. Press, Cambridge, U. K.

Prejean, S. G., and W. L. Ellsworth (2001), Observations of earthquake source parameters at 2 km depth in the Long Valley Caldera, Eastern California, *Bull. Seismol. Soc. Am., 91*(2), 165–177.

Rayleigh, L. (1917), On the pressure developed in a liquid during the collapse of a spherical bubble, *Philos. Mag., 34,* 94–98.

Robie, R. A., and B. S. Hemingway (1995), Thermodynamic properties of minerals and related substances at 298.15 K and 1 bar (10^5 Pascals) pressure and at higher temperatures, *U. S. Geol. Surv. Bull., 2132,* 461.

Roman, C. N., and H. Singh (2007), A self-consistent bathymetric mapping algorithm, *J. Field Rob., 24*(1–2), 23–50.

Rona, P. A., Y. A. Bogdanov, E. G. Gurvich, A. Rimski-Korsakov, A. M. Sagalevitch, M. D. Hannington, and G. Thompson (1993a), Relict hydrothermal zones in the TAG hydrothermal field, Mid-Atlantic Ridge 26°N, 45°W, *J. Geophys. Res., 98*(B6), 9715–9730.

Rona, P. A., M. D. Hannington, C. V. Raman, G. Thompson, M. K. Tivey, S. E. Humphris, C. Lalou, and S. Petersen (1993b), Active and relict seafloor hydrothermal mineralization at the TAG hydrothermal field Mid-Atlantic Ridge, *Econ. Geol., 18,* 1989–2017.

Ross, A., G. R. Foulger, and B. R. Julian (1996), Non-double-couple earthquake mechanisms at The Geysers geothermal area, California, *Geophys. Res. Lett., 23*(8), 877–880.

Scherer, G. W. (1999), Crystallization in pores, *Cem. Concr. Res., 29,* 1347–1358.

Scherer, G. W. (2004), Stress from crystallization of salt, *Cem. Concr. Res., 34,* 1613–1624, doi:10.1016/j.cemconres.2003.12.034.

Scholz, C. H. (2002), *The Mechanics of Earthquakes and Faulting,* Cambridge Univ. Press, Cambridge, U. K.

Seyfried, W. E., Jr. (1987), Experimental and theoretical constraints on hydrothermal alteration processes at mid-ocean ridges, *Ann. Rev. Earth Planet. Sci., 15,* 317–335.

Šílený, J., D. P. Hill, L. Eisner, and F. H. Cornet (2009), Non-double-couple mechanisms of microearthquakes induced by hydraulic fracturing, *J. Geophys. Res., 114,* B08309, doi:10.1029/2008JB005987.

Sleep, N. H. (1991), Hydrothermal circulation, anhydrite precipitation, and thermal structure at ridge axes, *J. Geophys. Res., 96*(B2), 2375–2387.

Sohn, R. A. (2007a), Stochastic analysis of exit fluid temperature records from the active TAG hydrothermal mound (Mid-Atlantic Ridge, 26°N): 1. Modes of variability and implications for subsurface flow, *J. Geophys. Res., 112,* B07101, doi:10.1029/2007JB004435.

Sohn, R. A. (2007b), Stochastic analysis of exit fluid temperature records from the active TAG hydrothermal mound (Mid-Atlantic Ridge, 26°N): 2. Hidden Markov models of flow episodes, *J. Geophys. Res., 112,* B09102, doi:10.1029/2007JB004961.

Sohn, R. A., J. A. Hildebrand, S. C. Webb, and C. G. Fox (1995), Hydrothermal microseismicity t the Megaplumes ite on the southernJ uan de Fuca Ridge, *Bull Seismol. Soc., 85,* 775–786.

Sohn, R., D. Fornari, K. Von Damm, J. Hildebrand, and S. Webb (1998), Seismic and hydrothermal evidence for a cracking event on the East Pacific Rise crest at 9°50′N, *Nature, 396,* 159–161.

Sohn, R. A., J. A. Hildebrand, and S. C. Webb (1999), A microearthquake survey of the high-temperature vent fields on the volcanically active East Pacific Rise (9°50′N), *J. Geophys. Res., 104*(B11), 25,367–25,377.

Sohn, R. A., A. H. Barclay, and S. C. Webb (2004), Microearthquake patterns following the 1998 eruption of Axial Volcano, Juan de Fuca Ridge: Mechanical relaxation and thermal strain, *J. Geophys. Res.*, *109*, B01101, doi:10.1029/2003JB002499.

Song, F., H. S. Kuleli, M. N. Toksöz, E. Ay, and H. Zhang (2010), An improved method for hydrofracture-induced microseismic event detection and phase picking, *Geophysics*, *75*(6), A47–A52, doi:10.1190/1.3484716.

Steiger, M. (2005a), Crystal growth in porous materials—I: The crystallization pressure of large crystals, *J. Cryst. Growth*, *282*, 455–469, doi:10.1016/j.jcrysgro.2005.05.007.

Steiger, M. (2005b), Crystal growth in porous materials—II: Influence of crystal size on the crystallization pressure, *J. Cryst. Growth*, *282*, 470–481, doi:10.1016/j.jcrysgro.2005.05.008.

Stroup, D. F., D. F. Bohnenstiehl, \M. Tolstoy, F. Waldhauser, and R. T. Weekly (2007), Pulse of the seafloor: Tidal triggering of microearthquakes at 9°50′N, *Geophys. Res. Lett.*, *34*, L15301, doi:10.1029/2007GL030088.

Teagle, D. A. H., J. C. Alt, H. Chiba, S. E. Humphris, and A. N. Halliday (1998), Strontium and oxygen isotopic constraints on fluid mixing, alteration and mineralization in the TAG hydrothermal deposit, *Chem. Geol.*, *149*, 1–24.

Tivey, M. K., S. E. Humphris, G. Thompson, M. D. Hannington, and P. A. Rona (1995), Deducing patterns of fluid flow and mixing within the active TAG mound using mineralogical and geochemical data, *J. Geophys. Res.*, *100*(B7), 12,527–12,555.

Tivey, M. K., R. A. Mills, and D. A. H. Teagle (1998), Temperature and salinity of fluid inclusions in anhydrite as indicators of seawater entrainment and heating in the TAG active mound, in *Proceedings of the Ocean Drilling Program, Scientific Results*, vol. 158, edited by P. M. Herzig et al., pp. 179–190, Ocean Drilling Program, College Station, Tex.

Tivey, M. A., H. Schouten, and M. C. Kleinrock (2003), A near-bottom magnetic survey of the Mid-Atlantic Ridge axis at 26°N: Implications for the tectonic evolution of the TAG segment, *J. Geophys. Res.*, *108*(B5), 2277, doi:10.1029/2002JB001967.

Tolstoy, M., F. L. Vernon, J. A. Orcutt, and F. K. Wyatt (2002), Breathing of the seafloor: Tidal correlations of seismicity at Axial volcano, *Geology*, *30*, 503–506, doi:10.1130/0091-7613(2002)030<0503:BOTSTC>2.0.CO;2.

Tolstoy, M., F. Waldhauser, D. R. Bohnenstiehl, R. T. Weekly, and W.-Y. Kim (2008), Seismic identification of along-axis hydrothermal flow on the East Pacific Rise, *Nature*, *451*, 181–185, doi:10.1038/nature06424.

Van Dover, C. L. (1995), Ecology of Mid-Atlantic Ridge hydrothermal vents, in *Hydrothermal Vent Processes*, vol. 87, edited by L. M. Parson, C. L. Walker, and J. B. D. R. Dixon, pp. 257–294, *Spec. Publ. Geol. Soc. London*, London, U. K.

Van Dover, C. L., B. Fry, J. F. Grassle, S. Humphris, and P. A. Rona (1988), Feeding biology of the shrimp *Rimicaris exoculata* at hydrothermal vents on the Mid-Atlantic Ridge, *Mar. Biol.*, *98*, 209–216.

Vandemeulebrouck, V., P. Roux, P. Gouédard, A. Legaz, A. Revil, A. W. Hurst, A. Bolève, and A. Jardani (2010), Application of acoustic noise and self-potential localization techniques to a buried hydrothermal vent (Waimangu Old Geyser site, New Zealand), *Geophys. J. Int.*, *180*, 883–890.

Vermilye, J. M., and C. H. Scholz (1995), Relation between vein length and aperture, *J. Struct. Geol.*, *17*(3), 423–434.

Violay, M., B. Gibert, D. Mainprice, B. Evans, J.-M. Dautria, P. Azais, and P. Pezard (2012), An experimental study of the brittle-ductile transition of basalt at oceanic crust pressure and temperature conditions, *J. Geophys. Res.*, *117*, B03213, doi:10.1029/2011JB008884.

Walder, J., and B. Hallet (1985), A theoretical model of the fracture of rock during freezing, *Geol. Soc. Am. Bull.*, *96*, 336–346.

Webb, S. C. (1992), The equilibrium oceanic microseism spectrum, *J. Acoust. Soc. Am.*, *92*(4), 2141–2158.

Webb, S. C., and W. C. Crawford (1999), Long-period seafloor seismology and deformation under ocean waves, *Bull. Seismol. Soc. Am.*, *89*(6), 1535–1542.

White, S. N., S. E. Humphris, and M. C. Kleinrock (1998), New observations on the distribution of past and present hydrothermal activity in the TAG area of the Mid-Atlantic Ridge (26°08′N), *Mar. Geophys. Res.*, *20*, 41–56.

Wichers, S., H. Singh, and R. Reves-Sohn (2005), Verification of numerical models for hydrothermal plume water through field measurements at TAG, Thesis (S.M.)--Joint Program in Applied Ocean Science and Engineering, Massachusetts Institute of Technology, Dept. of Ocean Engineering; and the Woods Hole Oceanographic Institution, Cambridge, Mass.

Wilcock, W. S. D. (2001), Tidal triggering of microearthquakes on the Juan de Fuca Ridge, *Geophys. Res. Lett.*, *28*(20), 3999–4002.

Wilcock, W. S. D., and D. R. Toomey (1991), Estimating hypocentral uncertainties for marine microearthquake surveys: A comparison of the generalized inverse and grid search methods, *Mar. Geophys. Res.*, *13*, 161–171.

Wilcock, W. S. D., S. D. Archer, and G. M. Purdy (2002), Microearthquakes on the Endeavour segment of the Juan de Fuca Ridge, *J. Geophys. Res.*, *107*(B12), 2336, doi:10.1029/2001JB000505.

You, C. F., and M. J. Bickle (1998), Evolution of an active sea-floor massive sulphide deposit, *Nature*, *394*, 668–671.

Zhao, M., J. P. Canales, and R. A. Sohn (2012), Three-dimensional seismic structure of a Mid-Atlantic Ridge segment characterized by active detachment faulting (Trans-Atlantic Geotraverse, 25°55′N-26°20′N), *Geochem., Geophys., Geosyst.*, *13*, Q0AG13, doi:10.1029/2012GC004454.

Zonenshain, L. P., M. I. Kuzmin, A. P. Lisitsin, Y. A. Bogdanov, and B. V. Baranov (1989), Tectonics of the Mid-Atlantic rift valley between the TAG and MARK areas (26–24°N): Evidence for vertical tectonism, *Tectonophysics*, *159*, 1–23.